Design study for MCAO deployable IFUs: sensitivities and source structures

Ivan K. Baldry and Keith Taylor

October 20, 2000

One of the instruments planned for use with multi-conjugate adaptive optics (MCAO) on Gemini includes a deployable integral-field unit (IFU) spectrograph. This report considers some of the issues associated with source sensitivity.

Contents

1 Signal-to-noise ratio calculations

Deployable IFUs for MCAO will have apertures of around $0.1'' \times 0.1''$ with spectral resolving powers of around 2000 to 5000. This enters a regime where detector dark current, readout noise and sky background can all contribute about equally to the final noise characteristics. The factors that need to be included in any calculation of the noise characteristics are shown in Table 1.

Table 1: Parameters used for limiting sensitivity and signal-to-noise ratio calculations

description	symbol	typical value	units
total integration time on object	T	14400	seconds
required S/N (or achieved S/N)	R_{req}	10	
primary-mirror area	A	50	m^2
total efficiency	e	0.20	
detector dark current	d	0.01	electrons s^{-1} pix^{-1}
detector readout noise	N_r	3.0	electrons pix^{-1}
individual frame integration time	t	1800	seconds
average sky-OH flux in band	S_{oh}	18000	photons s^{-1} m^{-2} $arcsec^{-2}$ μm^{-1}
average sky-continuum flux	S_c	600	photons s^{-1} m^{-2} $arcsec^{-2}$ μm^{-1}
scattered light fraction	f_s	0.05	
IFU aperture width[a]	l	0.10	arcseconds
wavelength	λ	1.25	μm
spectral resolving power	$\mathcal{R}$	5000	
sampling per resolution element[b]	n_{pix}	4.0	pixels
sky-subtraction factor[c]	F_{ss}	1.2	
sky flux at observed wavelength	S	600	photons s^{-1} m^{-2} $arcsec^{-2}$ μm^{-1}
object flux	O	100	photons s^{-1} m^{-2} $arcsec^{-2}$ μm^{-1}

[a] assuming aperture is square, i.e., IFU aperture area is l^2
[b] sampling per spatial and spectral resolution element, e.g., $n_{pix} = 4$ with $0.05''$ pixels and $l = 0.10''$
[c] the factor times which the sky background contributes to the variance of the measured counts after sky subtraction: using beam switching, $F_{ss} = 2$, and; using mean-sky techniques, $F_{ss} \sim 1.1$ to 1.2.

The variance (not including the object flux contribution) for a single IFU aperture and a single spectral resolution element, after sky subtraction, can be written as

$$\sigma_s^2 = F_{ss}\, T \left[\frac{N_r^2\, n_{pix}}{t} \;+\; d\, n_{pix} \;+\; \frac{S\, A\, e\, l^2\, \lambda}{\mathcal{R}} \;+\; \frac{f_s (S_{oh} + S_c) A\, e\, l^2\, \lambda}{\mathcal{R}} \right] \tag{1}$$

assuming uniformly distributed scattered light. The four terms in the equation represent contributions from readout noise, dark current, sky background and scattered sky light.

To determine the signal-to-noise ratio (S/N) for an object, further factors need to be considered: intrinsic seeing and Strehl ratio defining the point-spread function (PSF); object flux, spectrum and spatial structure. For a uniform continuum source, the number of measured counts per resolution element is

$$\mathcal{N} = \frac{O\, T\, A\, e\, l^2\, \lambda}{\mathcal{R}} \tag{2}$$

and the S/N is

$$R = \frac{\mathcal{N}}{\sqrt{\mathcal{N} + f_s \mathcal{N} + \sigma_s^2}} \,. \tag{3}$$

To reach a required S/N, R_{req},

$$\mathcal{N} \geq \frac{(1+f_s)R_{req}^2 + \sqrt{(1+f_s)^2 R_{req}^4 + 4\sigma_s^2 R_{req}^2}}{2} \,. \tag{4}$$

All the above analysis is assuming that the systematic effects can be kept to a minimum during the integrations. For instance, dark current, scattered light and the sky must be subtracted without introducing significant systematic errors.

For uniform emission-line sources (unresolved lines), $O\lambda/\mathcal{R}$ in Equation 2 can be replaced by a single parameter O' (photons s^{-1} m^{-2} $arcsec^{-2}$).

For point sources and non-uniform extended sources, the PSF needs to be considered.

2 Night-sky OH spectrum

Important in any analysis of spectroscopy in the near infrared is the sky OH spectrum. We have used a list of identified line wavelengths and strengths to simulate sky OH spectra at different spectral resolutions. An example is shown in Figure 1 using Gaussian PSFs. In addition to the OH line list (originally compiled by F. Piché from various sources, e.g, Maihara et al. 1993), we added weaker OH lines between the identified lines to account for incompleteness. An estimate of the strength and number of these weaker lines was obtained by comparing the OH line list with the OH spectrum published by Rousselot et al. (2000).

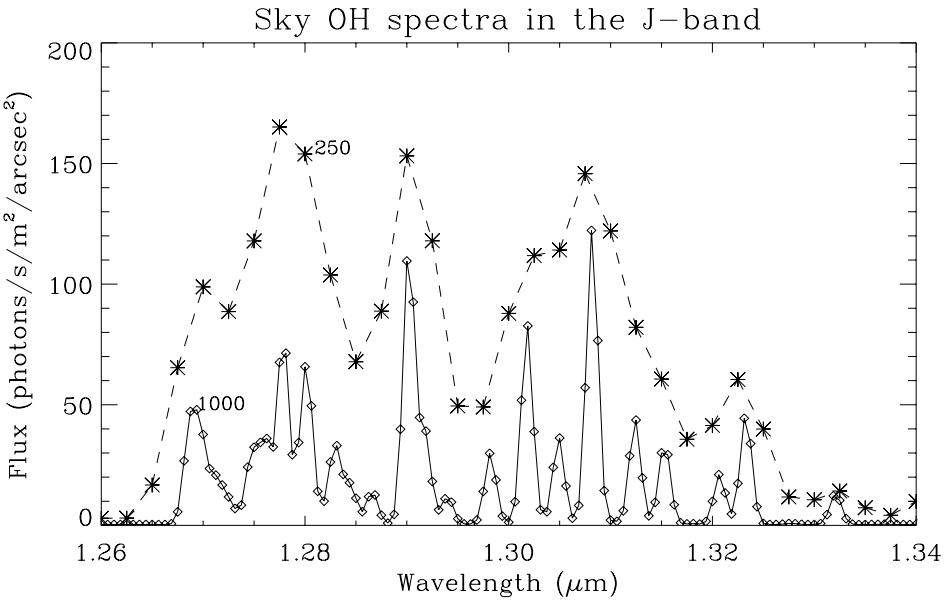

Figure 1: Simulated OH spectra in the J-band at two different resolutions ($\mathcal{R} = 250$ and 1000). The spectra are produced by convolving delta functions with Gaussian PSFs. Note that the flux is per spectral bin, with two bins per full width at half maximum (FWHM) of the Gaussians.

Haynes et al. (2000) plotted the OH-clear fraction versus spectral resolving power in the J and H bands. In Figure 2, we view the OH-clear part of the spectrum by sorting the emission at different spectral resolving powers from 100 to 30000. The spectra become 50% clear of OH lines at about $\mathcal{R} \sim 3000$ depending on how the OH-clear fraction is defined. The sky-continuum flux is taken to be 600 photons s^{-1} m^{-2} $arcsec^{-2}$ μm^{-1} (Maihara et al. 1993) in the J and H bands and increasing from about 700 to 3500 photons s^{-1} m^{-2} $arcsec^{-2}$ μm^{-1} across the K band (2–2.4 μm). The K band flux could be higher due to the thermal emissivity of an MCAO system. The average sky-OH fluxes across these bands are about 17000, 25000 and 2000 photons s^{-1} m^{-2} $arcsec^{-2}$ μm^{-1}, respectively.

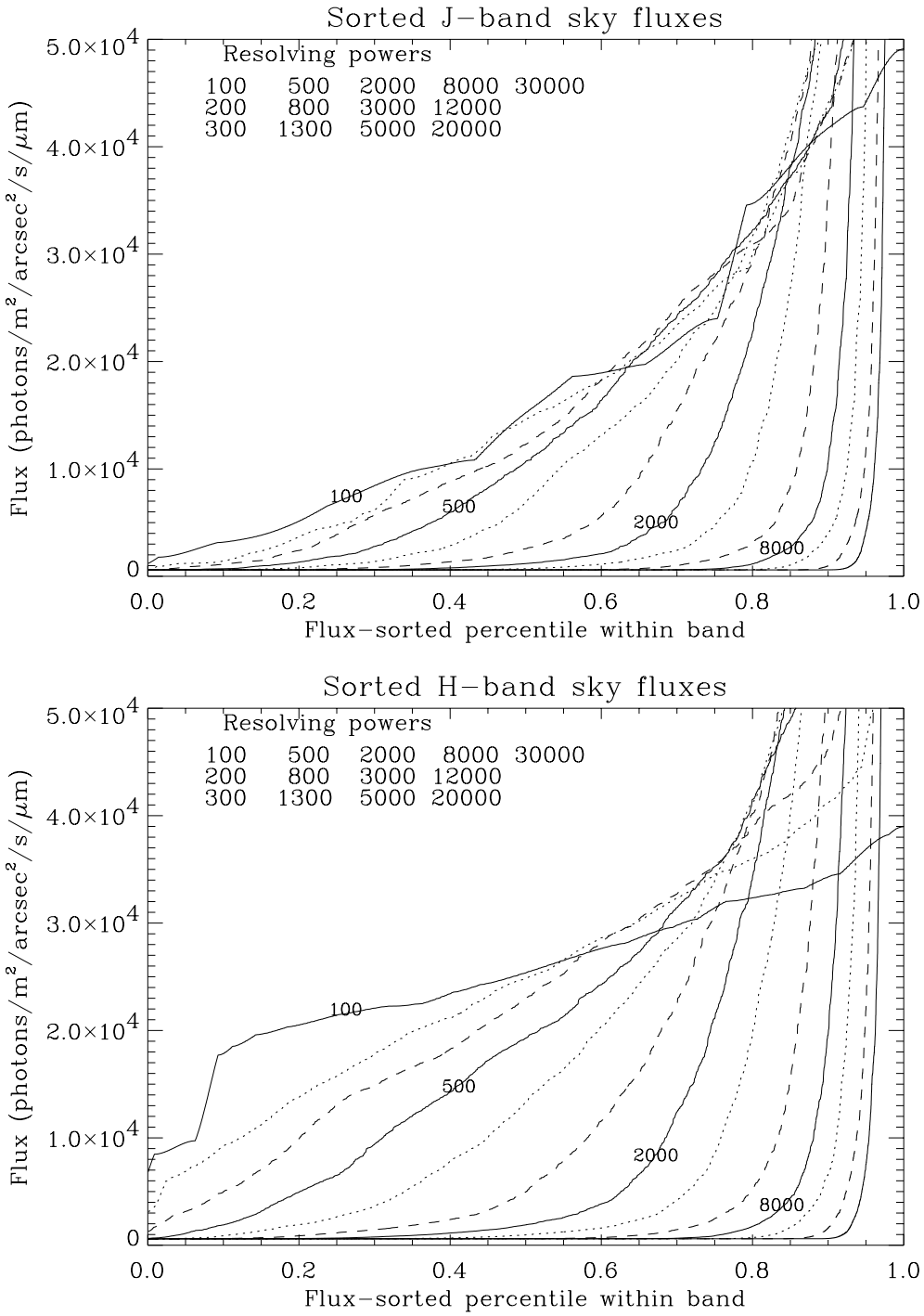

Figure 2: Simulated sky fluxes in the J- and H-bands at various resolving powers. The flux has been sorted within each band, e.g., the flux at a percentile of 0.5 corresponds to the median value. The mean flux is the same at all resolutions.

3 Continuum sensitivity

Sensitivity to approximately uniform continuum sources is, to first order, independent of the PSF at the telescope focal plane (assuming the sources are well resolved). Figure 3 shows the limiting surface brightnesses versus IFU aperture width and versus spectral resolving power. At small aperture widths ($l \lesssim 0.1''$), the sensitivity is strongly dependent on the detector noise. Due to these low surface brightness (SB) limits, an aperture width of around $0.1''$ is probably more useful than aperture widths that critically resolve MCAO PSFs ($l \sim 0.02''$ to $0.03''$). Additionally, an aperture width of about $0.1''$ gives the highest S/N in a single IFU aperture and spectral resolution element for point sources (Fig. 4).

Clearly, the limiting sensitivity decreases with increasing spectral resolving power, in terms of detecting continuum emission per resolution element. However, at higher spectral resolving power, more of the source is viewed through OH-clear regions. This means that spectra observed at high resolving power can be rebinned to a lower resolving power with increased sensitivity depending on detector noise. To test this, we performed numerical calculations assuming the spectra could be optimally rebinned to a lower resolution (using weighting). An example is shown in Figure 5. The S/N is improved in the OH sky regions but is reduced in OH-clear regions due to detector noise.

From these numerical calculations, we can determine an optimal spectral resolving power for OH suppression. A figure of merit is the gain in mean $(\mathrm{S/N})^2$. This can be normalized so that the gain factor at a particular resolving power is the $(\mathrm{S/N})^2$ on optimally filtering the entire band (i.e., forming an OH-suppressed broad-band image from the IFU data cube) relative to the $(\mathrm{S/N})^2$ of standard broad-band imaging. The gain in rebinning from a resolving power $X\mathcal{R}$ to $\mathcal{R}$, compared to observing at $\mathcal{R}$, is equal to the gain factor at $X\mathcal{R}$ divided by the gain factor at $\mathcal{R}$. Figure 6 shows the gain factor versus resolving power in the J and H bands with various detector-noise characteristics. Figure 7 shows the gain factor for the $zJHK$ bands with detector characteristics of $N_r = 3$ and $d = 0.01$ (Vural et al. 1999).

Thus, with the expected detector-noise characteristics and deployable IFUs for MCAO, there is no gain in observing above resolving powers of about 2000 in J and 3000 in H for continuum sensitivity at moderate resolving powers ($\mathcal{R} \lesssim 1000$).

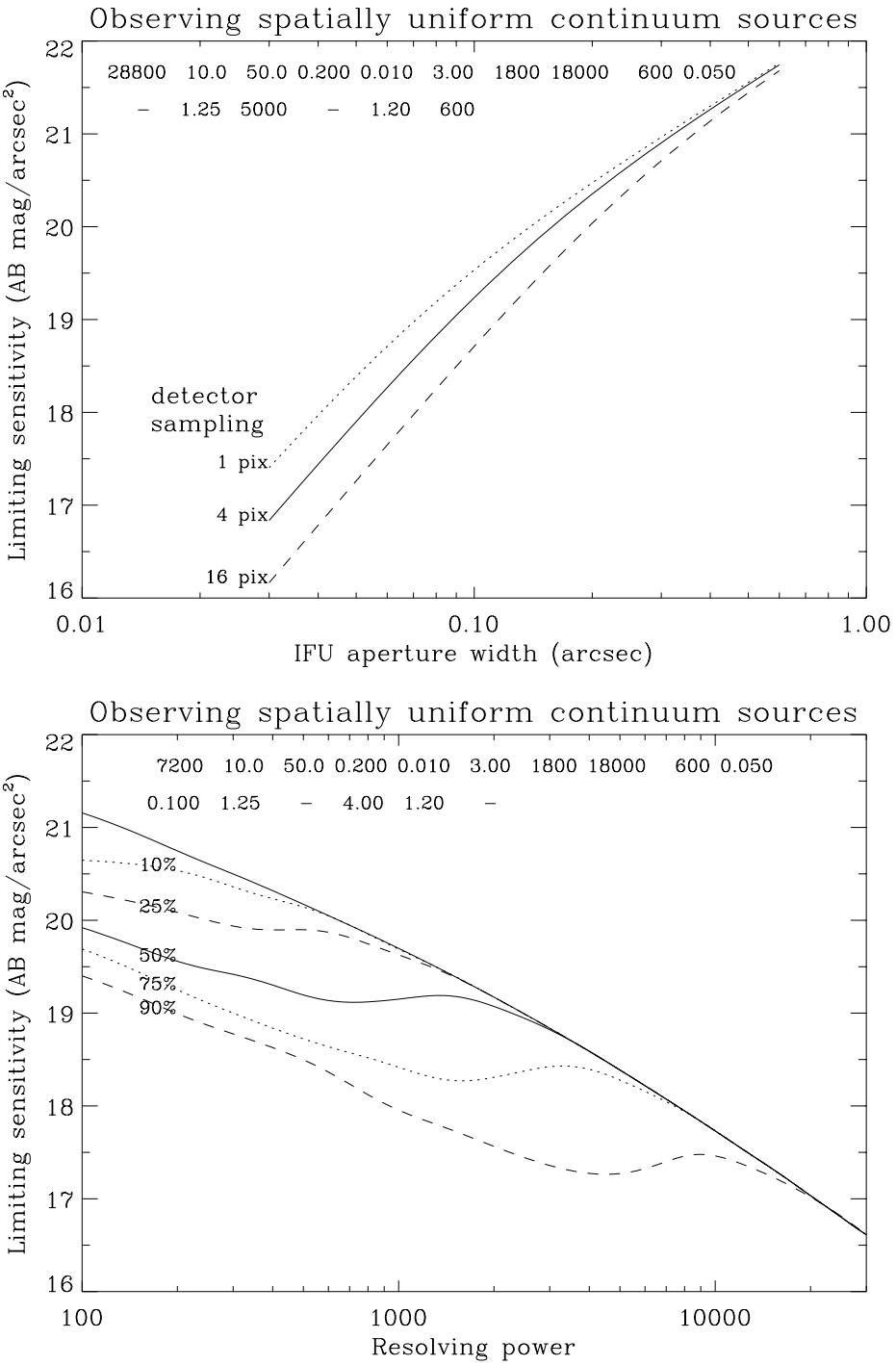

Figure 3: Limiting surface brightnesses for obtaining a S/N of ten in a single spatial and spectral resolution element. The upper plot shows surface brightness (SB) versus IFU aperture width (l) with three different sampling factors per resolution element (n_{pix}). The lower plot shows SB versus spectral resolving power ($\mathcal{R}$) with various sky fluxes (S) defined by the flux-sorted percentile (Fig. 2). The other factors used in the calculations are given in two rows: [T, R_{req}, A, e, d, N_r, t, S_{oh}, S_c, f_s], [l, λ, $\mathcal{R}$, n_{pix}, F_{ss}, S] defined in Table 1 (p. 2).

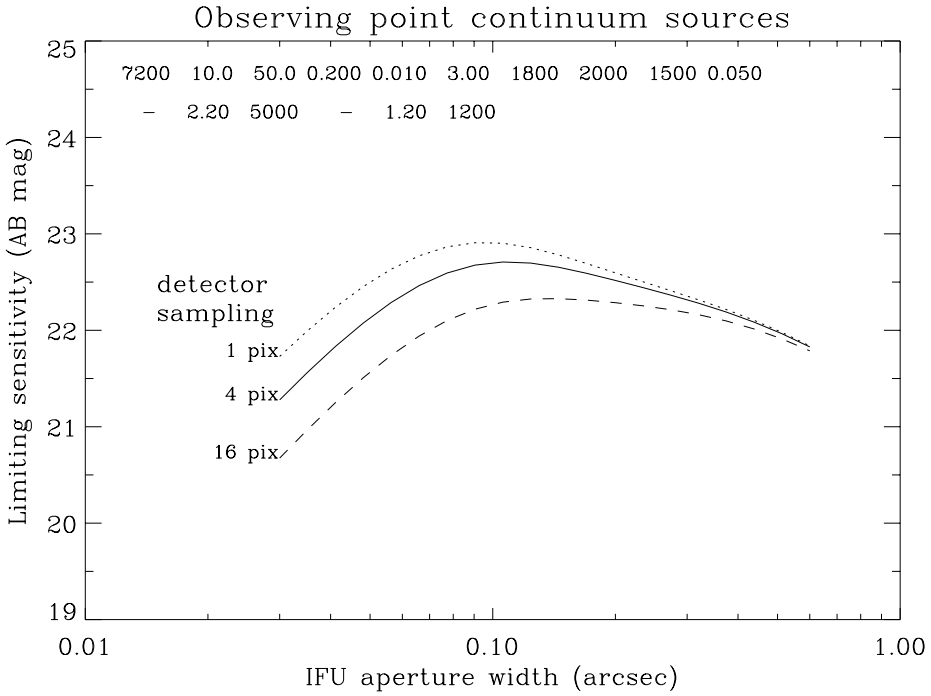

Figure 4: Limiting point-source magnitudes for obtaining a S/N of ten in a single spatial and spectral resolution element. See Figure 3 for details. A simple PSF model consisting of a narrow and a wide Gaussian was used to determine the aperture coupling.

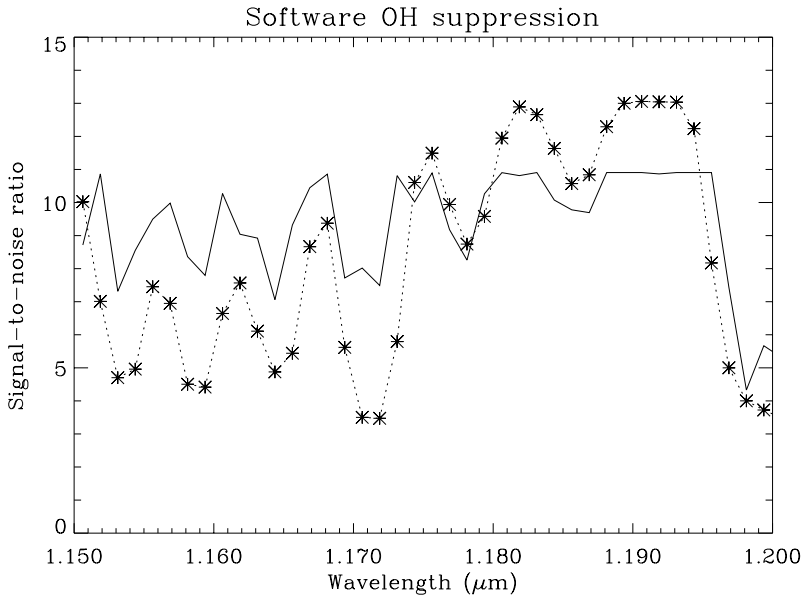

Figure 5: Simulation of software OH suppression. The dotted line represents the S/N of a continuum source observed at a spectral resolving power of 500. The solid line represents an observation taken at 2500 optimally rebinned to 500. While the S/N is reduced in the regions that were OH clear at the lower resolution (due to increased detector noise), the S/N is increased in most of the OH regions.

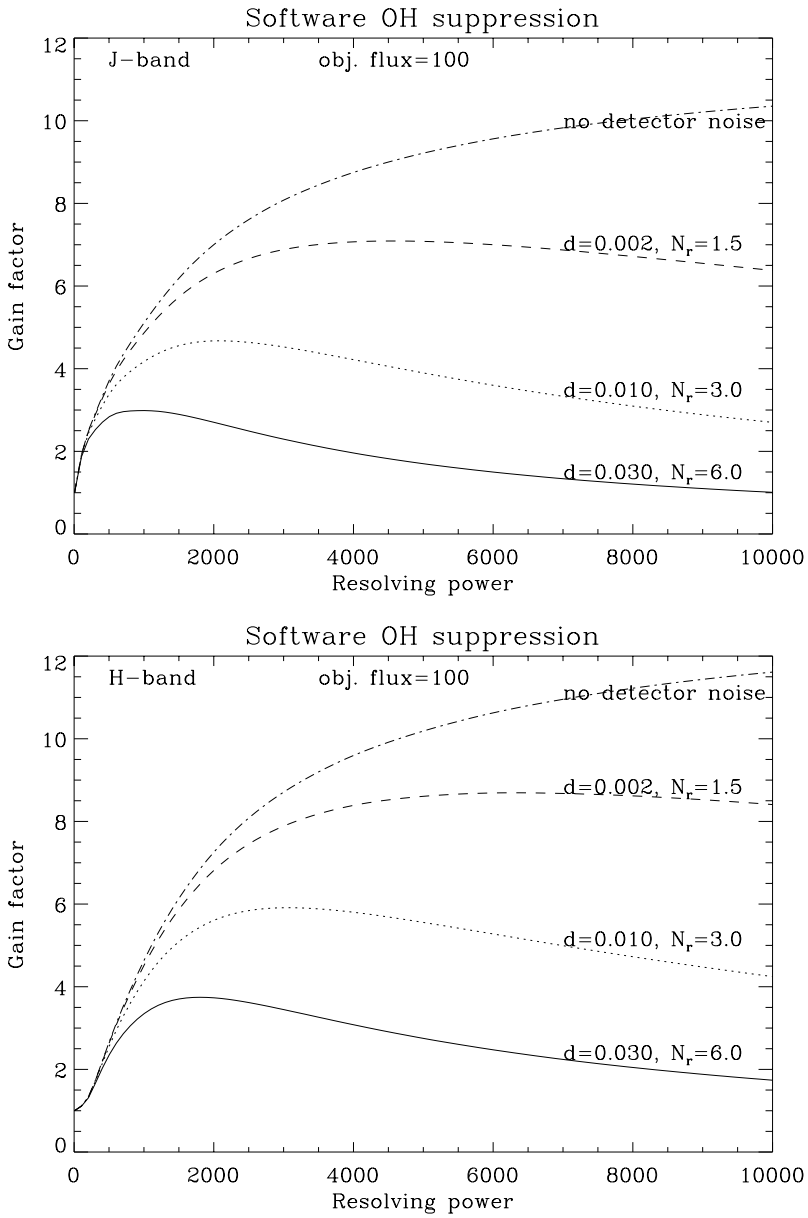

Figure 6: The gain factor for software OH suppression (optimally rebinning data to a lower spectral resolving power) in the J and H bands with various detector noise characteristics. The gain in mean $(\mathrm{S/N})^2$ when rebinning from a resolving power $X\mathcal{R}$ to $\mathcal{R}$, compared to observing at $\mathcal{R}$, is equal to the gain factor at $X\mathcal{R}$ divided by the gain factor at $\mathcal{R}$. For the lowest-background infrared arrays at present (dotted line), the peak in continuum sensitivity (rebinning to $\mathcal{R} \lesssim 1000$) is for observations with resolving powers of about 2000 in J and 3000 in H.

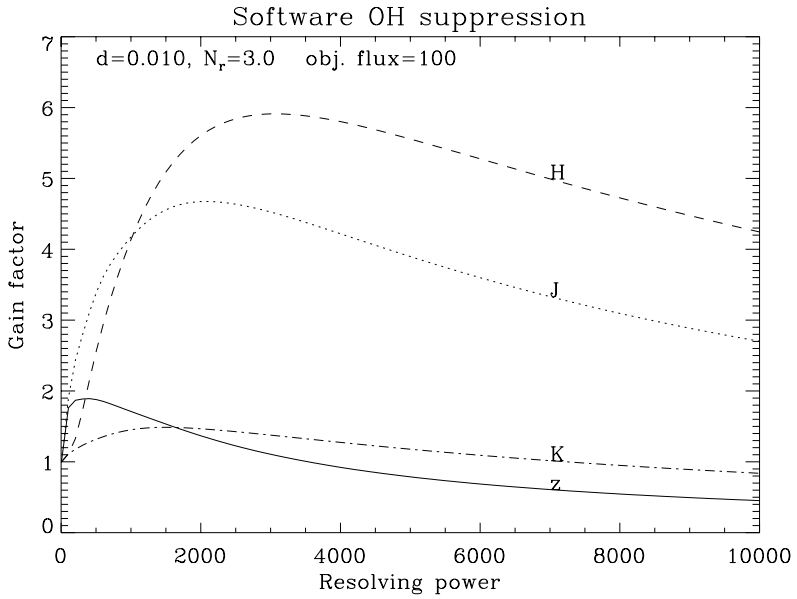

Figure 7: The gain factor for software OH suppression in the $zJHK$ bands. The band wavelength ranges are: z, 0.9–1.1 μm; J, 1.15–1.35 μm; H, 1.5–1.8 μm; K, 2.0–2.4 μm.

4 Emission-line sensitivity

The optimum resolving power for emission-line detection depends on the intrinsic width of the emission line as well as detector-noise and sky characteristics. For unresolved emission lines, the sensitivity increases with spectral resolving power until detector noise totally dominates (see Figure 8).

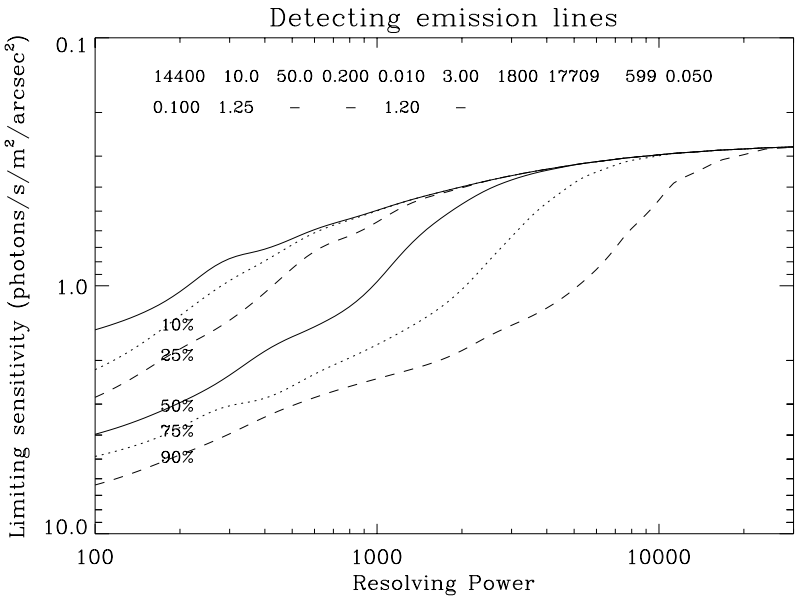

Figure 8: Sensitivity to unresolved emission lines versus spectral resolving power. Note that the y-axis unit values are reversed. The different lines represent the percentile sorted sky fluxes at different resolving powers (see Fig. 2), with the top solid line representing the sky continuum regions. The other factors used in the calculations are given in two rows: [T, R_{req}, A, e, d, N_r, t, S_{oh}, S_c, f_s], [l, λ, $\mathcal{R}$, n_{pix}, F_{ss}, S] defined in Table 1 (p. 2).

For resolved emission lines, the observed line width is approximately the instrumental PSF width added in quadrature with the intrinsic line width. The sensitivity increases with resolving power approximately until the object emission line is resolved, after which the sensitivity decreases due to an increasing detector noise contribution. The peak of sensitivity with spectral resolving power will depend on the intrinsic line width and the position of the OH lines in relation to the object emission line. Figure 9 shows sensitivity versus resolving power for two different line widths.

Note that unless object emission lines have FWHM less than $100\,\mathrm{km\,s^{-1}}$, there is little or no gain in observing with spectral resolving powers above 3000.

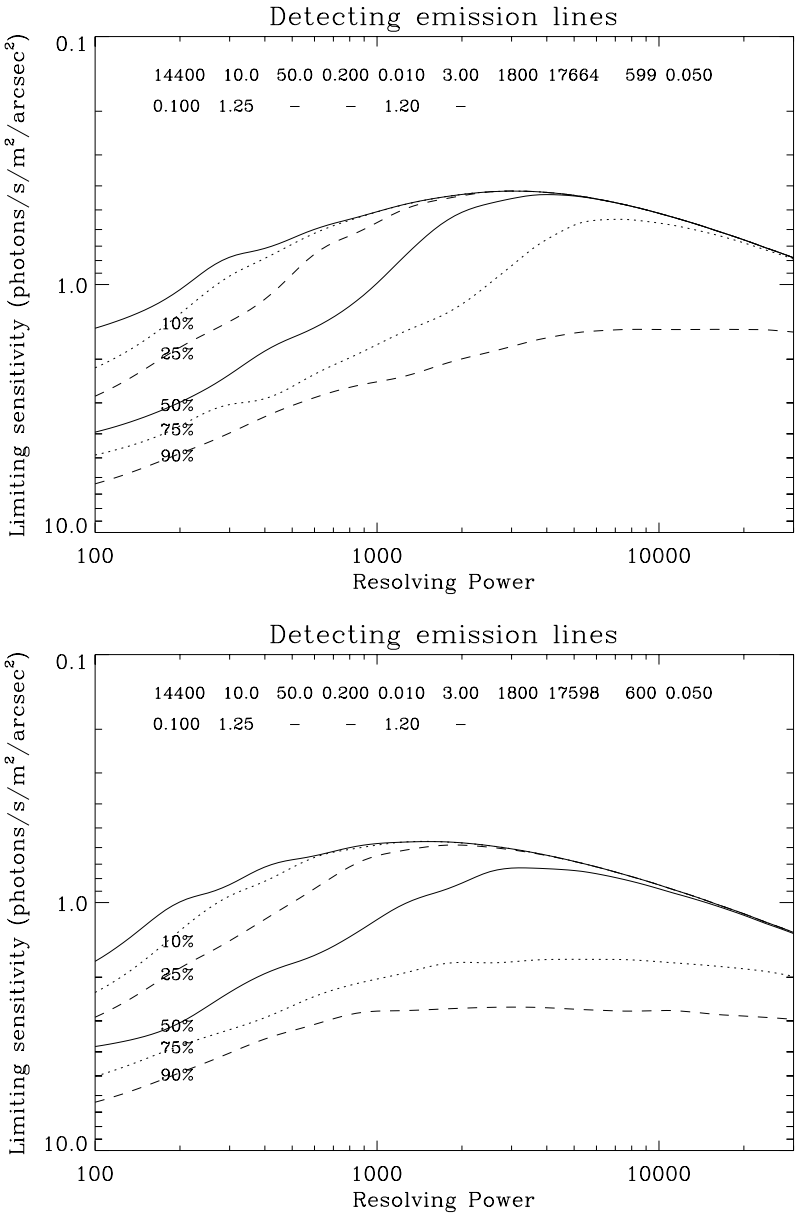

Figure 9: Sensitivity to resolved emission lines, with FWHM of $100\,\mathrm{km\,s^{-1}}$ (upper plot) and $300\,\mathrm{km\,s^{-1}}$ (lower plot). See Figure 8 for details.

5 Star-formation rate sensitivity

Hα emission is approximately proportional to the star-formation rate (SFR) for many galaxy systems. Conversion from SFR to photon flux at the Earth is described in Section B. From Equation 13 or 16, along with S/N calculations, it is possible to determine the required SFR for Hα emission detection as a function of redshift. This is shown in Figure 10 for a spectral resolving power of 3000. Note that the required SFR surface brightness in the units $M_\odot$ yr^{-1} Kpc^{-2} is independent of the cosmology.

The required SFR increases with Z due to the increase in luminosity distance and is higher in the OH regions of the sky spectrum. If the Hα emission coincides with an OH line, it may be easier to measure the SFR using another emission line. Other emission lines produced near star-forming regions are given in Section C.

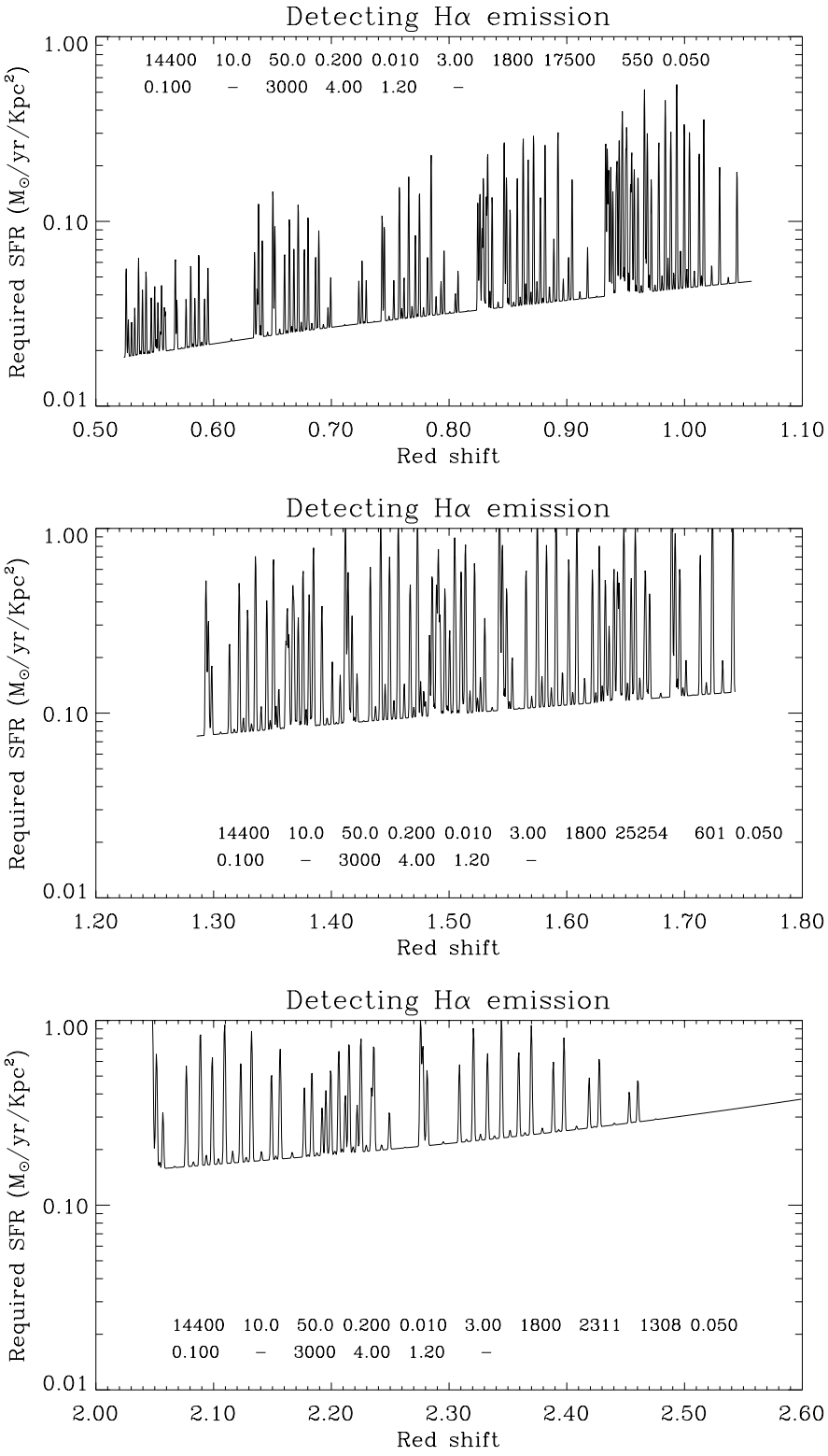

Figure 10: Required SFR to detect Hα emission with a S/N of ten in a single spatial and spectral resolution element (J, H and K bands), i.e., the limiting SFR sensitivity as a function of redshift of the host galaxy, assuming an approximately spatially uniform SFR and a conversion to Hα luminosity of 10^{34} W / ($\mathrm{M}_\odot\,\mathrm{yr}^{-1}$). The other factors used in the calculations are given in two rows: [T, R_{req}, A, e, d, N_r, t, S_{oh}, S_c, f_s], [l, λ, $\mathcal{R}$, n_{pix}, F_{ss}, S] defined in Table 1 (p. 2).

6 Testing using HDF galaxies

Galaxies in the Hubble Deep Field (HDF) can be used to predict the S/N in emission lines and continua observed using IFU spectroscopy with MCAO. Mark Dickinson kindly provided us with images of eighteen $Z = 2$–3 galaxies from the HDF. For each galaxy, two images were obtained by interpolation between observed passbands with WFPC2 and NICMOS, a rest-frame 1700Å image and a rest-frame 4300Å image (Dickinson 2000). The rest-frame UV image was used to predict the SFR (conversion given by Madau et al. 1998) and the strength of the emission lines in the near infrared. The SFRs varied between about 5 and 30 $\mathrm{M}_\odot\,\mathrm{yr}^{-1}$. The NICMOS images give the predicted continuum strengths.

The PSF of the WFPC2 images has a FWHM of around $0.14''$ which has approximately the same enclosed energy in a $0.1'' \times 0.1''$ aperture as MCAO. Therefore, to a first approximation, the images can be used without convolving with an MCAO PSF to predict the S/N of IFU spectra using MCAO. IFU spectra were simulated for all of the eighteen galaxies. In addition, the same galaxies were placed at other redshifts between 1 and 3, with redshift intervals of 0.5. In this redshift range, the length-to-angular scale is fairly constant for most cosmologies (Section D). Example simulated IFU spectra are shown in Figure 11. Note that the aperture width used was $0.12''$ to simplify rebinning from the drizzled WFPC2 pixel scale of $0.04''$.

The continuum is rarely detectable with a S/N of 3 for any of the high redshift galaxies (at spectral resolving powers of around 3000). Rebinning the spectra to $\mathcal{R}$ of 500 or 100 should allow measurement of the continua. The principle measurements will be of emission lines. Figure 12 shows the number of IFU elements for which the emission line S/N is greater than three and greater than ten, as a function of redshift, for Hα and [OIII] λ5007. The intrinsic width of the lines was assumed to be $100\,\mathrm{km\,s}^{-1}$.

For most of the high redshift ($Z > 1$) galaxies, IFU sizes of around $1''$ to $1.5''$ would be adequate. Our analysis of Dickinson's arrays used $1.8'' \times 1.8''$ IFUs. For nearer galaxies ($Z < 0.5$), larger IFUs are generally needed. Bob Abraham (via Ray Sharples) provided us with a spiral image of HDF-3.534 at $Z = 0.319$ (Abraham et al. 1999). Simulated IFU spectra from this image showed continuum detection in the brightest part of the galaxy and [SIII] λ9069/9532 emission line detection across much of the galaxy in a one hour exposure.

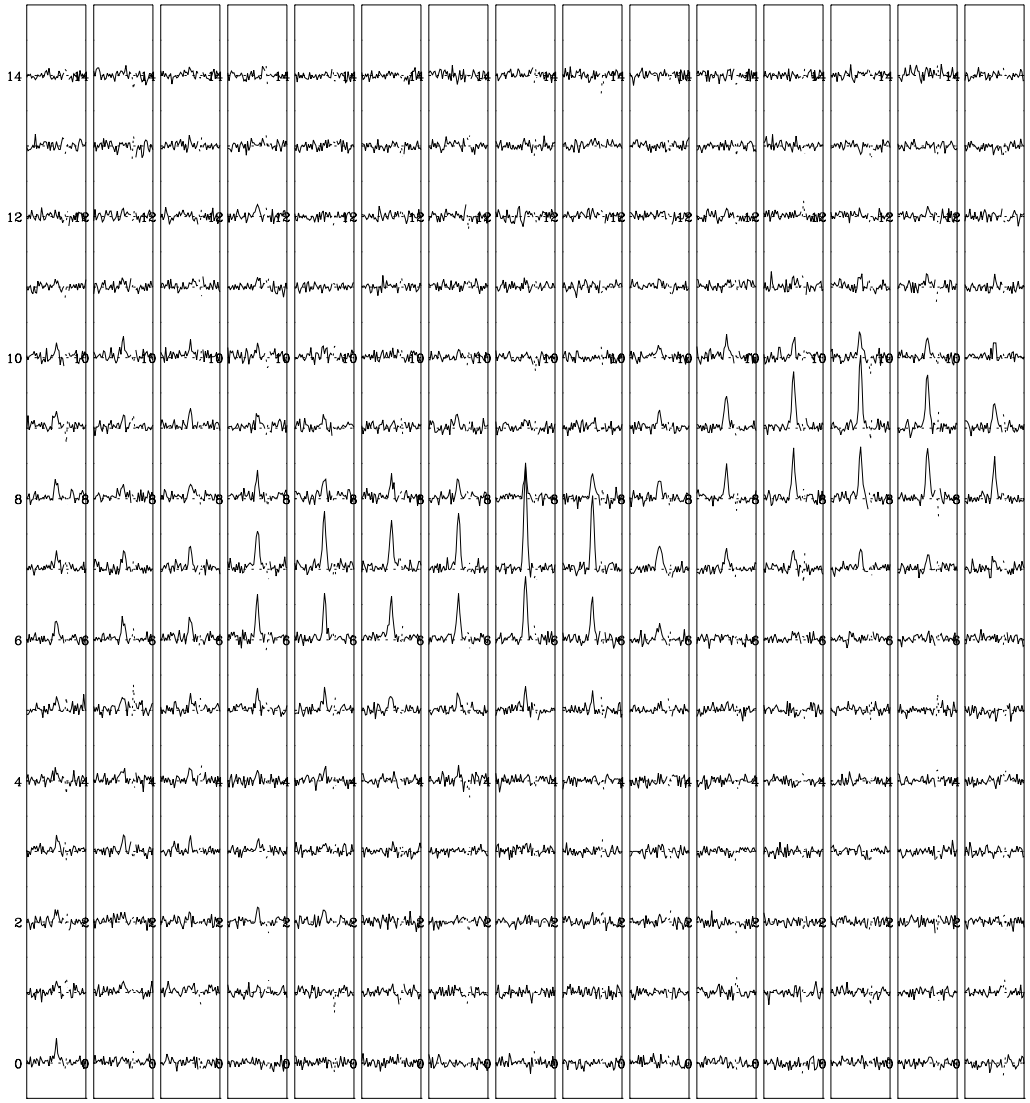

Figure 11: Simulated IFU spectra of the HDF 2-585.1 galaxy morphology at a redshift of 1.51 (galaxy is really at 2.01). The spectra show Hα emission in many of the IFU elements. The exposure time was 4 hours, the resolving power was 3000 and 0.12″ apertures were used.

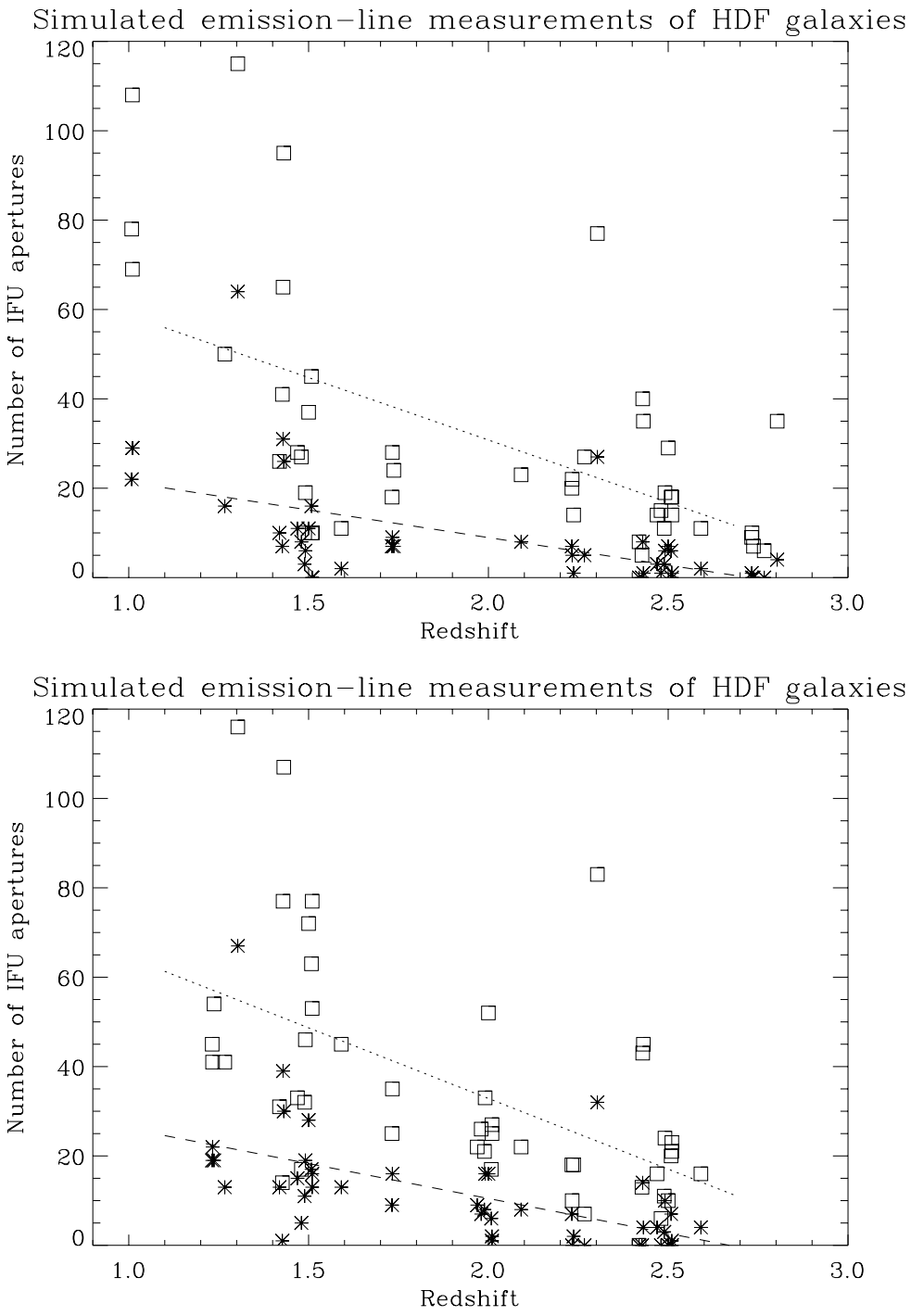

Figure 12: The number of IFU elements showing Hα emission (upper plot) and [OIII] λ5007 emission (lower plot) as a function of redshift. Each of the eighteen galaxies analysed by Dickinson (2000) were placed at their measured redshift plus at additional redshifts separated by 0.5 between $Z = 1$ and $Z = 3$. The squares represent the number of elements with S/N > 3, while the asterisks represent the number with S/N > 10. Note that the effect of OH lines is included, in the sense that if the emission falls on an OH line, the S/N is lower.

7 Testing by redshifting nearby galaxies

Another approach to simulating IFU spectra is to take images and data cubes of nearby galaxies and artificially place them at high redshift. This has the advantage that the spatial resolution (at high redshift) is much better than MCAO or WFPC2 and, therefore, the images can be convolved with appropriate PSFs for comparison between MCAO and single-conjugate adaptive optics (SCAO). The disadvantage is that the morphologies of high redshift ($Z > 1$) are generally different to nearby galaxies.

Pat Shopbell and Joss Bland-Hawthorn kindly provided us with a Fabry-Perot Hα & [NII] data cube of M82 (Shopbell & Bland-Hawthorn 1998) for our S/N calculations. Increasing the size of the galaxy and redshifting to $Z = 0.8$ (J band) and $Z = 2.1$ (K band), we simulated IFU spectra including the spatial convolution with a range of PSFs (at different points in the field of view) for MCAO and SCAO. Figure 13 shows example IFU spectra for the J band using off-axis PSFs. An aperture width of $0.11''$ was used.

For each PSF, we determined the maximum S/N in the IFU spectra and the RMS S/N for the Hα emission across the 8×8 apertures shown in Figure 13. Figure 14 shows a comparison between MCAO and SCAO. The maximum S/N drops significantly for off-axis SCAO compared to MCAO but the RMS S/N only drops slightly due to the spreading of light over more pixels in the SCAO case. There is less difference between the two adaptive-optics systems in the K band.

To test the difference in spatial resolution between MCAO and SCAO, we simulated the Hα flux in a series of IFU apertures from an Hα image of M83 provided by Sonia Cianci and Joss Bland-Hawthorn. The IFU images are shown in Figure 15 for two different off-axis positions. The galaxy image does not resemble a spiral when viewed off axis by $42''$ with SCAO.

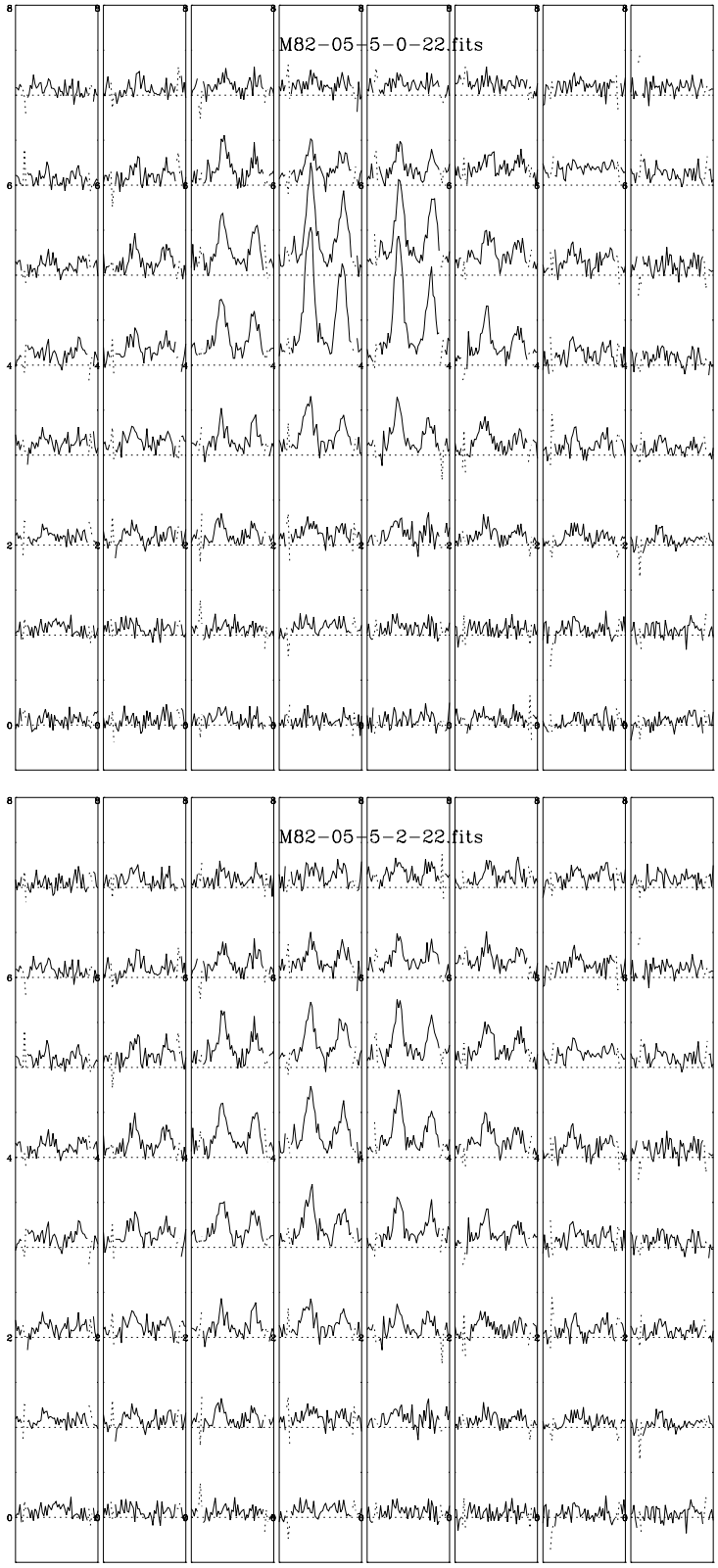

Figure 13: Simulated IFU spectra using a data cube of M82 projected to a redshift of 0.8 and convolved with off-axis (by 42″) PSFs: MCAO (upper plot) and SCAO (lower plot). The spectra show Hα and [NII] emission. The maximum S/N is lower for SCAO.

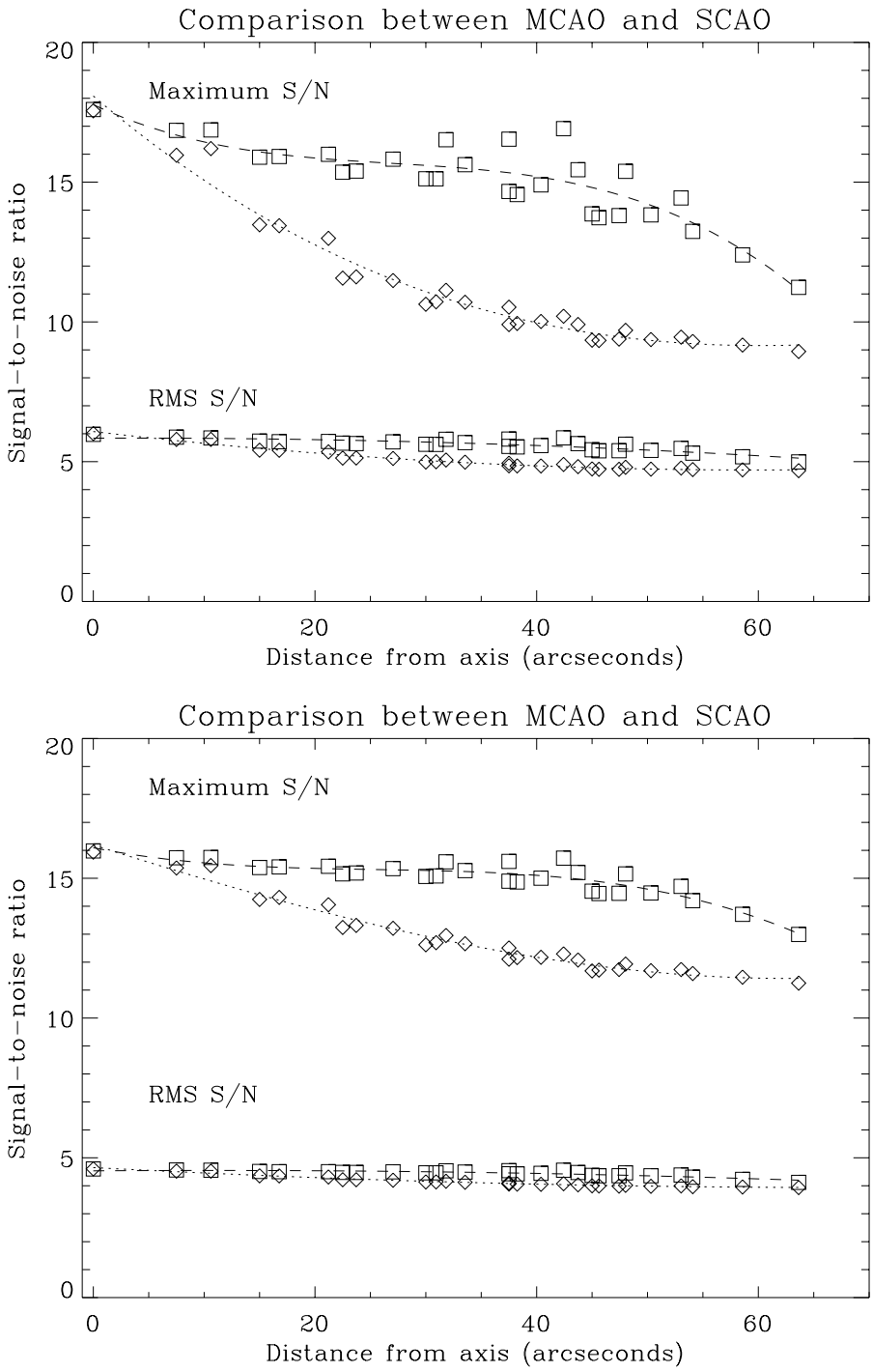

Figure 14: Comparison between MCAO and SCAO in the J band (upper plot) and the K band (lower plot). The maximum S/N in the IFU data cube are plotted for various PSFs (squares represent MCAO and diamonds represent SCAO). The RMS S/N for Hα emission across the central part of the image (see Fig. 13) is also shown. Note that the object flux was increased for the K band analysis to obtain a similar S/N at the higher redshift.

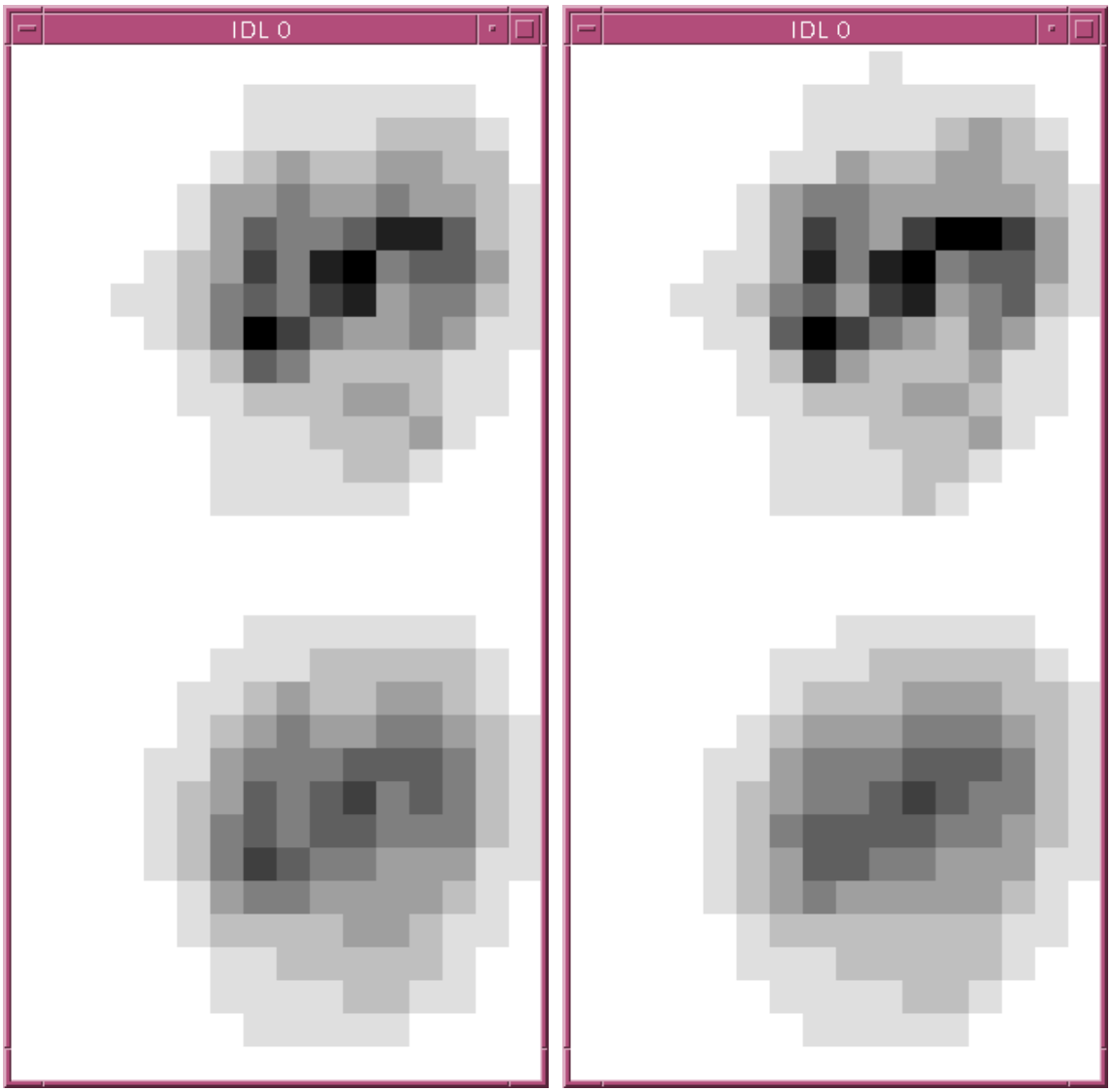

Figure 15: Simulated Hα images of a high redshift spiral. An Hα image of M83 was placed at $Z \sim 1$ and convolved with off-axis adaptive-optics PSFs in the J band. The upper images represent MCAO and the lower images represent SCAO, with the left images taken off axis by $22''$ and the right images by $42''$. The pixel scale is $0.11''$.

A Conversion between continuum-flux units

Converting between photon flux, energy flux and magnitudes is not readily obvious. A couple of useful formulas to remember are:

$$f_\nu = 6.626 \times 10^{-8}\, \lambda\, f'_\lambda \tag{5}$$

and;

$$\mathrm{AB} = -2.5 \log f_\nu + 8.9 \tag{6}$$

where

- f_ν is the energy flux measured in Jy (Janskys, equivalent to 10^{-26} W m^{-2} Hz^{-1}),
- λ is the wavelength measured in μm,
- f'_λ is the photon flux measured in photons s^{-1} m^{-2} μm^{-1},
- AB is the magnitude scale defined by Oke & Gunn (1983)[1].

The conversion to standard magnitudes depends on the calibration of the Vega flux in different wavelength bands. An example is shown below for the Johnson-Cousins-Glass photometric system (Bessell 1992).

band	B	V	R	I	J	H	K	L	M
effective wavelength (μm)	0.436	0.545	0.638	0.797	1.22	1.63	2.19	3.45	4.75
zeroth mag flux (Jy)	4000	3600	3060	2420	1570	1020	636	281	154

Example conversions for fluxes at various wavelengths are shown in Table 2, the Vega magnitudes are approximated using a fit to the above calibrations.

Table 2: Conversions between continuum-flux units in the near infrared

wavelength (μm)	photon flux (s^{-1} m^{-2} μm^{-1})	energy flux (μJy)	AB mag	band	Vega mag
1.00	100	6.6	21.8	(z)	21.2
1.00	1000	66.3	19.3	(z)	18.7
1.25	100	8.3	21.6	J	20.6
1.25	1000	82.8	19.1	J	18.1
1.65	100	10.9	21.3	H	19.9
1.65	1000	109.3	18.8	H	17.4
2.20	100	14.6	21.0	K	19.1
2.20	1000	145.8	18.5	K	16.6

[1] note that there is a sign error in the formula given in the paper

B Conversion between SFR and Hα flux

The total Hα luminosity of a galaxy can be written as

$$L = k\,\mathcal{S} \tag{7}$$

where k is a constant calibrated from observations and $\mathcal{S}$ is the star-formation rate (SFR). From Kennicutt (1983), $k = 1.1 \times 10^{34}\,\mathrm{W}\ /\ (\mathrm{M}_\odot\ \mathrm{yr}^{-1})$, and; from Alonso-Herrero et al. (1996), $k = 3.1 \times 10^{34}$. Differences between calibrations partially depend on the initial mass function. To convert to luminosity measured in photons s^{-1},

$$L' = k\,\mathcal{S}\,\frac{\lambda}{h_p c} \tag{8}$$

where λ is the rest wavelength of Hα, h_p is Planck's constant and c is the speed of light. The flux received at Earth is given by

$$F' = \frac{L'}{4\pi[R_0 S_k(r)]^2(1+Z)} \tag{9}$$

where Z is the red shift and $R_0 S_k(r)$ is the effective distance. Note that there is only a single factor of $1+Z$ because we are dealing with flux measured in photons s^{-1} rather than Watts. The effective distance can be written as

$$R_0 S_k(r) = \frac{c}{H_0}\hat{D} \tag{10}$$

where $\hat{D}$ is a dimensionless distance which, for a matter-dominated universe, is given by (Peacock 1999)

$$\hat{D} = \frac{2}{\Omega^2(1+Z)}\left[\Omega Z + (\Omega - 2)\left(\sqrt{1+\Omega Z} - 1\right)\right]\ ; \tag{11}$$

H_0 is the Hubble constant and Ω is the density parameter at the present time. The flux can then be written as

$$F' = \frac{k\mathcal{S}\lambda H_0^2}{4\pi c^3 h_p}\frac{1}{\hat{D}^2(1+Z)}\,. \tag{12}$$

In SI units: $k\mathcal{S} \sim 10^{34}\,\mathrm{W}$ (for a SFR of about one solar mass per year); $\lambda = 6.563 \times 10^{-7}\,\mathrm{m}$; $h^{-1}H_0 = 3.241 \times 10^{-18}\,\mathrm{s}^{-1}$; $c = 2.998 \times 10^8\,\mathrm{m\,s}^{-1}$; $h_p = 6.626 \times 10^{-34}\,\mathrm{J\,s}$. Combining the constants, we get

$$F' = 0.307\frac{K\mathcal{S}h^2}{\hat{D}^2(1+Z)}\,\mathrm{photons\,s}^{-1}\,\mathrm{m}^{-2} \tag{13}$$

where: $K = k/[10^{34}\,\mathrm{W}\ /\ (\mathrm{M}_\odot\ \mathrm{yr}^{-1})]$, a factor of order unity relating Hα luminosity to SFR; $\mathcal{S}$ is the SFR in solar masses per year; h is the Hubble parameter, and; $\hat{D}$ is a cosmological-distance parameter.

Alternatively, the equation for photon flux can be written as

$$F' = \frac{k\mathcal{S}\lambda}{4\pi c h_p}\frac{(1+Z)}{D_L^2}\,, \tag{14}$$

where D_L is the luminosity distance:

$$D_L = (1+Z)R_0 S_k(r)\,. \tag{15}$$

With appropriate units, the photon flux is given by

$$F' = 2.76 \times 10^6\frac{K\mathcal{S}(1+Z)}{(D_L/\mathrm{Mpc})^2}\,\mathrm{photons\,s}^{-1}\,\mathrm{m}^{-2}\,. \tag{16}$$

C Nebular lines in the near infrared

MCAO IFU spectroscopy of high redshift galaxies ($Z \gtrsim 0.5$) will principally involve the detection and measurement of emission lines from gas clouds heated by star formation regions. Continuum detection is difficult due to the low surface brightness of these galaxies and star-formation rates will almost certainly be high for detected high redshift galaxies. Madau et al. (1998) showed that the SFR density of the universe is significantly higher between $Z = 0.5$ and $Z = 4$ compared to the present, peaking at around $Z = 1.5$.

The principal emission lines that could be detected in the JHK bands between redshifts 0.5 and 4 are OII λ3727, Hγ λ4340, Hβ λ4681, OIII λ4959/5007, Hα λ6563, NII λ6548/6583, SII λ6716/6730, SIII λ9069/9532, HeI λ10830, Paβ λ12818. Figure 16 shows which near-IR bands some of these lines can be detected in as a function of redshift. Notably, there are opportunity windows where several of the lines will be visible in the three different bands (here defined as 1.1–1.35 μm, 1.5–1.8 μm and 2.0–2.4 μm). These windows are $Z = 0.68$–0.98, $Z = 1.29$–1.64, $Z = 2.09$–2.57 and $Z = 3.12$–3.79.

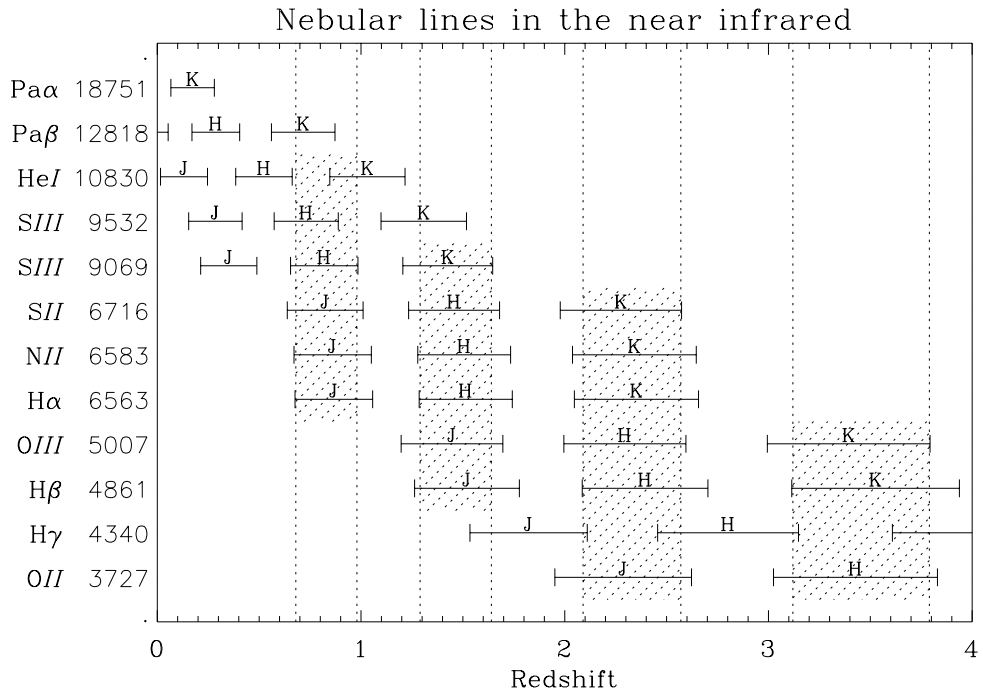

Figure 16:

D Length-to-angular scale for various cosmologies

From Peacock (1999), the relationship between angle on the sky and distance, as a function of redshift, can be determined. Figure 17 shows the length scale for various cosmologies. Notably, between redshifts of about $Z = 0.5$ and $Z = 5$, the scale varies by less than $\pm 25\%$ from an average value for the cosmologies shown. With $0.1''$ IFU apertures, distances of around 500–1000 parsecs can be resolved at high redshift.

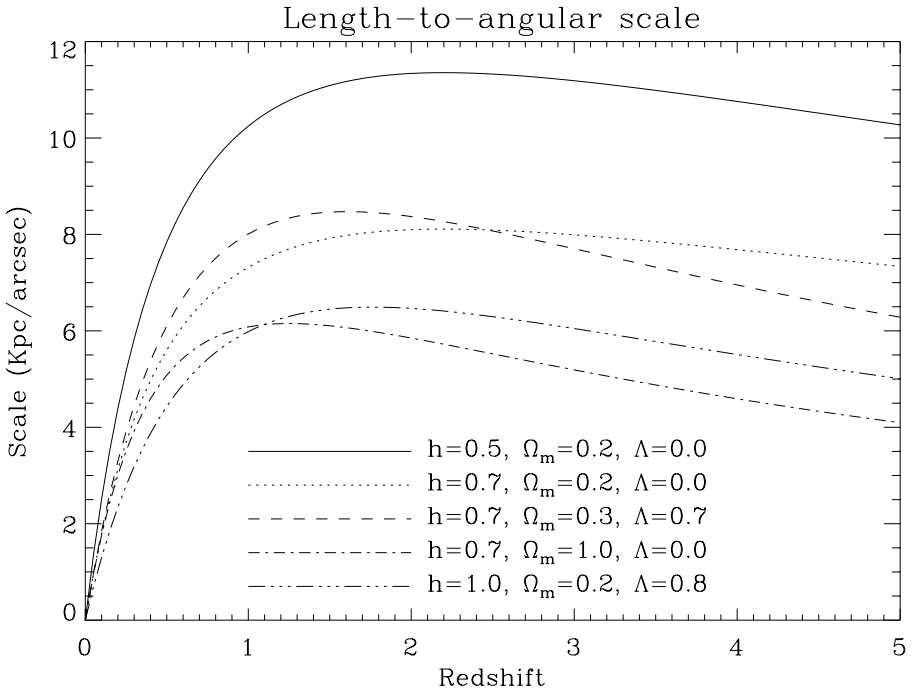

Figure 17:

Acknowledgments

We would like to thank: Bob Abraham, Joss Bland-Hawthorn, Sonia Cianci, Mark Dickinson, Chip Kobulnicky and Pat Shopbell for kindly providing galaxy images; Scott Croom, Karl Glazebrook, Alice Shapley, Ray Sharples, Chuck Steidel and others for various discussions, and; Francois Rigaut for the PSF models.

References

Abraham R. G., Ellis R. S., Fabian A. C., Tanvir N. R., Glazebrook K., 1999, The star formation history of the Hubble sequence: spatially resolved colour distributions of intermediate-redshift galaxies in the Hubble Deep Field, in **MNRAS, 303,** p. 641–658.

Alonso-Herrero A., Aragon-Salamanca A., Zamorano J., Rego M., 1996, Star formation history in a sample of starburst galaxies, in **MNRAS, 278,** p. 417–436.

Bessell M. S., 1992, Magnitude scales and photometric systems, in **The Astronomy and Astrophysics Encyclopedia,** ed. by Maran S. P., publ. by Van Nostrand Reinhold, New York, p. 403–407.

Dickinson M., 2000, The first galaxies: structure and stellar populations, in **Philosophical Transactions of the Royal Society, Series A,** astro-ph/0004028.

Haynes R., Baldry I. K., Taylor K., Lee D., 2000, Characterisation of cooled infrared fibres for the Gemini IRMOS, in **Proc. SPIE, 4008,** p. 1203–1214.

Kennicutt R. C., 1983, The rate of star formation in normal disk galaxies, in **ApJ, 272,** p. 54–67.

Madau P., Pozzetti L., Dickinson M., 1998, The star formation history of field galaxies, in **ApJ, 498,** p. 106–116.

Maihara T., Iwamuro F., Yamashita T., Hall D. N. B., Cowie L. L., Tokunaga A. T., Pickles A., 1993, Observations of the OH airglow emission, in **PASP, 105,** p. 940–944.

Oke J. B., Gunn J. E., 1983, Secondary standard stars for absolute spectrophotometry, in **ApJ, 266,** p. 713–717.

Peacock J. A., 1999, **Cosmological Physics,** publ. by Cambridge Univ. Press.

Rousselot P., Lidman C., Cuby J. G., Moreels G., Monnet G., 2000, Night-sky spectral atlas of OH emission lines in the near-infrared, in **A&A, 354,** p. 1134–1150.

Shopbell P. L., Bland-Hawthorn J., 1998, The Asymmetric Wind in M82, in **ApJ, 493,** p. 129–153.

Vural K., Kozlowski L. J., Cooper D. E. et al., 1999, 2048x2048 HgCdTe focal plane arrays for astronomy applications, in **Proc. SPIE, 3698,** p. 24–35.